Pump−Probe Simulation Study of the Two-Exciton Manifold of Dendrimers†

Andreas Tortschanoff and Shaul Mukamel*

Department of Chemistry, University of Rochester, Rochester, New York 14627

Received: August 18, 2001; In Final Form: October 23, 2001

The doorway window representation of sequential four wave mixing combined with the nonlinear exciton equations (NEE) is used to calculate femtosecond pump probe spectra of the dendrimeric nanostar. Direct signatures of exciton funneling and the two-exciton states are identified. The frequency-domain pump−probe signal is computed as well, showing the effects of exciton coupling and excited-state absorption. Further information obtained from different polarization configurations of the pulses with respect to the molecular orientation is discussed.

I. Introduction

The highly ordered branched macromolecules known as dendrimers have attracted much theoretical and experimental attention recently.[1−6] Their unique tree-like geometry makes them potential candidates for a wide variety of applications, including electrooptical organic light sources,[7] drug delivery[8] and nanoscale optical sensors.[9,10]

We consider dendrimers in which the various segments have an energy gradient from the periphery toward the center. Phenylacetylene dendrimers are one class of such molecules: The energy gradient can be designed by increasing the length of the phenylacetylene units in each generation.[11−15] Excitation energy can then be transferred very efficiently, similar to the primary steps in photosynthesis, where the excitation energy is transferred from the supramolecular antenna to the reactive center by means of multistep transport processes following an energy gradient. It was shown theoretically that ordered "Cayley trees" constitute an excellent energy funnel.[10,16−18]

In this paper we study a phenylethynylperylene-terminated derivative, known as the nanostar[10] (Figure 1), where one of the three dendrimer branches is substituted by a perylene-unit which can act as an exciton trap, collecting the photoexcited electron−hole pairs initially formed in the dendrimer. Recent experimental and theoretical investigations[18−23] have shown that the excitons are localized on the linear segments because the meta-branching on the phenylene-bridges inhibits effective delocalization. This makes it possible to model the optical response of this system using a Frenkel exciton Hamiltonian[24] with purely Coulombic coupling between excitations which reside on the linear segments.

In a series of recent studies, we have computed the electronic excitations, linear absorption, and stationary pump probe spectra.[21−23] The Frenkel Hamiltonian parameters were obtained using the collective electronic oscillator (CEO) approach.[23] The signatures of energy funneling in the time- and frequency-gated fluorescence signal were studied[18] by solving the equations of motions for a hierarchy of exciton oscillators (Nonlinear exciton equations).[25] Exciton transport was described using Redfield theory[26,27] where the effects of nuclear motion are incorporated through relaxation superoperators, calculated perturbatively in exciton−phonon coupling. The fluorescence signal was calculated in the doorway window representation of sequential four wave mixing spectroscopies,[28,29] which separates the dynamics into three distinct steps: Preparation of a doorway

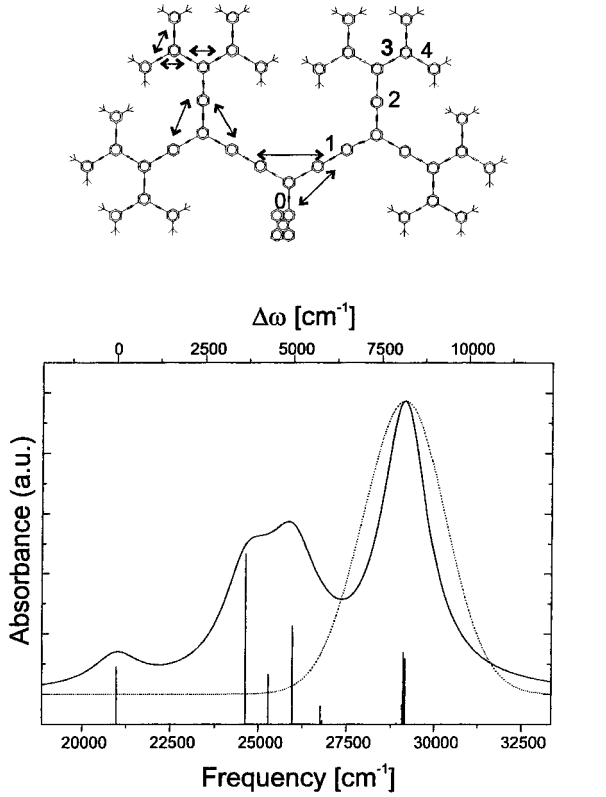

Figure 1. Top: The nanostar. Arrows indicate the couplings between adjacent segments used in the Frenkel Hamiltonian. The generation numbers are given. The site energies of the different generations are $\Omega_0 = 21\,011$ cm^{-1}, $\Omega_1 = 25\,058$ cm^{-1}, $\Omega_2 = 26\,347$ cm^{-1}, $\Omega_3 = \Omega_4 = 29\,044$ cm^{-1} and the transition dipole moments $\mu_0 = 1.47\ \mu_4$, $\mu_1 = 2.06\ \mu_4$, $\mu_2 = 1.67\ \mu_4$, $\mu_3 = \mu_4$. The excitonic couplings between different generations are $J_{01} = -302$ cm^{-1}, $J_{12} = -325$ cm^{-1}, $J_{23} = -158$ cm^{-1}, $J_{34} = 69$ cm^{-1} and within the same generation $J_{11'} = 326$ cm^{-1}, $J_{22'} = 347$ cm^{-1}, $J_{33'} = -72$ cm^{-1}, $J_{44'} = -69$ cm^{-1}. Bottom: The simulated absorption spectrum (solid line) together with the power spectrum of the excitation pulse (dotted line). The stick spectrum shows the individual one-exciton energies and oscillator strengths.

† Part of the special issue "G. Wilse Robinson Festschrift".

* To whom correspondence should be addressed. Fax: +1-716-473-6889. E-mail: mukamel@chem.rochester.edu.

10.1021/jp013221f CCC: $22.00 © xxxx American Chemical Society
Published on Web 00/00/0000 PAGE EST: 8.9

wave packet of excitons, subsequent evolution during a controlled time-delay, and finally computing the signal as the overlap of the doorway with a second (window-) wave packet which depends on the probe. The same procedure will be applied here to compute two-color pump probe spectra.

Nonlinear experiments such as pump−probe yield additional information not available from time-resolved fluorescence, in particular, direct information about two-exciton dynamics. Single color pump probe experiments on nanostars were reported recently.[30] The coupling and interactions among the segments may be also probed in the frequency domain. Stationary pump probe spectra are calculated as well using the nonlinear third-order susceptibility.

In section II, we summarize the expressions used for the calculation of the pump−probe signal, and the time-resolved pump−probe spectra are presented in section III. Section IV presents stationary pump−probe calculations and polarized pump−probe signals are discussed in section V.

II. Doorway-Window Representation of the Pump−Probe Signal

The extended nanostar, shown in Figure 1 together with its absorption spectrum can be modeled as an aggregate consisting of interacting two level systems, described by the Frenkel-exciton Hamiltonian[23]

$$H \equiv H_e + H_{ph} + H_{int} - E(t)P \tag{1}$$

H_e describes the electronic system

$$H_e \equiv \sum_{m,n} h_{mn} B_m^\dagger B_n \tag{2}$$

where $B_m^\dagger$ and B_m are the creation and annihilation operators of an exciton localized on the m'th linear segment (chromophore), which satisfy the Pauli commutation relations $[B_n, B_m^\dagger] = \delta_{mn}(1 - 2B_m^\dagger B_m)$. $h_{mn} \equiv \Omega_m \delta_{mn} + J_{mn}$, Ω_m is the exciton energy of the m'th linear segment and J_{mn} represents the exciton transfer matrix elements. The nanostar has four generations 1, 2, 3, 4 which together with the trap (generation 0) have 31 segments. Ω_m and J_{mn} were calculated in ref 23 and are given in the caption of Figure 1.

The single-exciton states are the eigenvalues (ϵ_α) and eigenvectors (φ_α) of the single exciton block of the Hamiltonian h_{mn}

$$\sum_n h_{mn}\varphi_\alpha(n) = \epsilon_\alpha \varphi_\alpha(m) \tag{3}$$

$\varphi_\alpha(m)$ represents the amplitude of the m'th segment on the delocalized exciton α.

The harmonic phonon bath Hamiltonian is

$$H_{ph} = \sum_\nu \left(\frac{p_\nu^2}{2m_\nu} + \frac{m_\nu \omega_\nu^2 q_\nu^2}{2} \right) \tag{4}$$

and the system-bath interaction is taken to be

$$H_{int} = \sum_{\nu,m,n} q_\nu \bar{\Omega}_{m,n,\nu} \bar{B}_m^\dagger \bar{B}_n \tag{5}$$

where q_ν, p_ν, m_ν and ω_ν are the coordinate, momentum, mass and frequency, of the ν'th bath oscillator, respectively. $\bar{\Omega}_{m,n,\nu}$ describes the vibronic coupling originating from the q_ν dependence of h_{mn}. In the Redfield theory of relaxation, the effects of the bath are introduced through relaxation superoperators describing the evolution of the reduced electronic density matrix.[31−33] The Redfield matrix was calculated by assuming that each linear segment of the nanostar is coupled to a single collective bath coordinate characterized by the overdamped Brownian oscillator spectral density

$$C(\omega) = 2\lambda \frac{\Lambda \omega}{\Lambda^2 + \omega^2} \tag{6}$$

Here, Λ is the nuclear relaxation rate and λ is the exciton−phonon coupling strength.

The last term in eq 1 describes the coupling with the external electric field, where P is the polarization operator

$$P = \sum_n \mu_n (B_n^\dagger + B_n) \tag{7}$$

and μ_m is the transition dipole moment of the m'th segment. In pump−probe spectroscopy the electric field is given by

$$E(t) = \epsilon_1(t)\exp(-i\omega_1 t) + \epsilon_2(t-\tau)\exp(-i\omega_2 t) + c.c. \tag{8}$$

with the pump-pulse complex envelope $\epsilon_1(t)$ centered around $t = 0$; the probe $\epsilon_2(t - \tau)$ is centered around $t = \tau$, and ω_1, ω_2 are the corresponding carrier frequencies.

The pump−probe signal S_{pp} can generally be written in terms of the third-order polarization $P^{(3)}(t)$[29]

$$S_{pp}(\tau,\omega_2) = \mathrm{Re}\int_{-\infty}^{\infty} dt\, \epsilon_2^*(t-\tau) P^{(3)}(t)\exp(i\omega_2 t) \tag{9}$$

We assume that the pump and probe pulses are well separated temporally so that the process is sequential i.e., the system first interacts with a pump and the signal is produced by a subsequent interaction with a delayed probe. Under these conditions, the signal can be calculated using the doorway window formalism.[32] (Additional coherent terms need to be added when the two pulses overlap;[34] these will not be included here.) The doorway-window expression for the sequential pump−probe signal is given by[29,32]

$$S_{pp}(\tau,\omega_1,\omega_2) = \sum_{mnkl} \int_0^\infty d\tau' \int_0^\infty dt'\, \mathscr{W}'_{mn}(\tau - \tau',\omega_2) \times G^{(N)}_{mn,kl}(t')\mathscr{D}_{kl}(\tau' - t',\omega_1) \tag{10}$$

$\mathscr{D}_{kl}$ is the *doorway wave packet*, representing the reduced one-exciton density matrix prepared by the pump. $\mathscr{W}'_{mn}$ is the *window wave packet* created from the ground, the one- and the two-exciton states, by two interactions with the probe. The Green function $G^{(N)}_{mn,kl}(t') \equiv \theta(t')\langle B_l(0)B_n^\dagger(t')B_m(t')B_l^\dagger(0)\rangle$ represents the propagation of the doorway during the delay period τ between pump and probe.

This representation provides an intuitive physical description that naturally separates the process into preparation, propagation and detection of the excitonic wave packet. The doorway wave packet contains the initially prepared exciton populations and coherences. Its propagation during the delay period τ between pump and probe is described by $G^{(N)}$ and the signal is given by the Liouville space overlap of the window with the propagated wave packet N_{mn}

$$N_{mn}(\tau) = \sum_{kl} \int_0^\infty dt' G^{(N)}_{mn,kl}(t')\mathscr{D}_{kl}(\tau - t',\omega_1) \tag{11}$$

The general expressions for $\mathscr{D}_{kl}$ and $\mathscr{W}'_{mn}$ depend on the single excitons Green functions G_{mn} and the scattering matrix $\bar{\Gamma}$. The

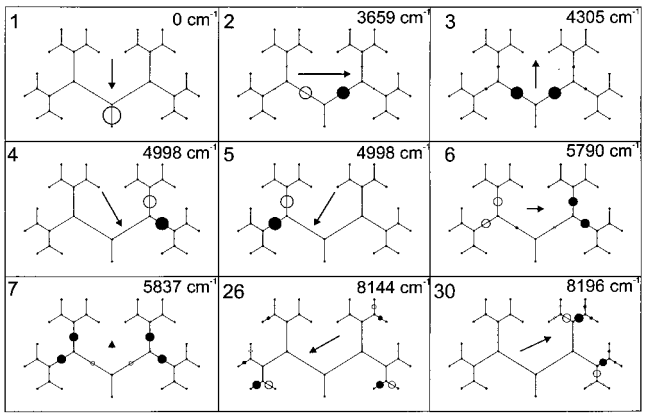

Figure 2. Wave functions $\varphi_\alpha(m)$ of single exciton states α. Shown are the first seven excitons and the two peripheric excitons with the largest oscillator strength, together with their relative energy. Numbering corresponds to Figure 3. Open (solid) circles indicate negative (positive) values with diameters proportional to $\varphi_\alpha(m)$. The direction and length of the arrows indicate the direction and size of the corresponding transition dipole moments to the ground state.

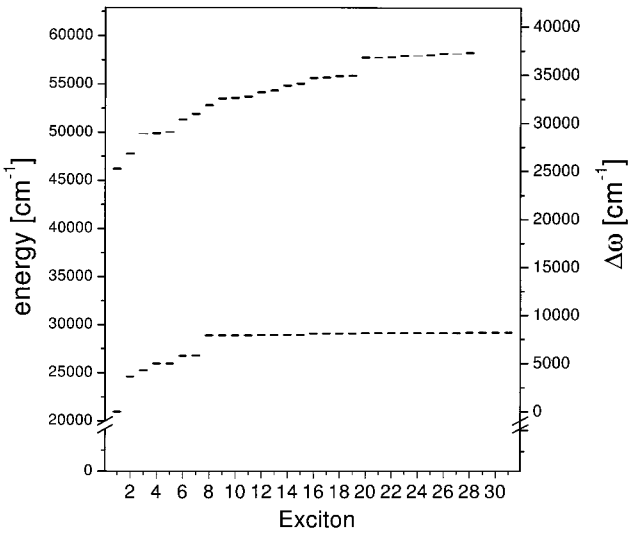

Figure 3. Energies and relative energies ($\Delta\omega$) of the single and two-exciton states.

simplify considerably in the *snapshot limit* where the laser pulses are short compared with the exciton dynamics time scale and long compared with the electronic dephasing time scale.[29,35] These are given in the appendix.

The transient pump probe signal of an aggregate has three contributions with distinct Liouville space pathways: (i) Hole burning (HB) and (ii) stimulated emission (SE) which arise from ground-state depletion and excited-state population and (iii) excited-state absorption (ESA) which results from transitions from the one-exciton to the two-exciton manifold. ESA gives a positive signal whereas HB and SE both give a negative signal. In our calculations, they are lumped together and we will refer to their sum as photobleaching (PB). More elaborate models, that include different dynamics in the ground and the excited state would allow to distinguish between these contributions. This however, goes beyond the scope of this article.

Because in our model, the energy gap between single- and two-exciton states ω_{fe} is similar to the transition energies between ground- and single-exciton states ω_{eg} (cf. Figure 3) the PB and ESA resonant pump−probe signals will appear in the same frequency region. In the present formulation, the two-exciton states are not calculated explicitly but the signal is directly obtained from the nonlinear exciton equations and expressed using the exciton scattering matrix.[25] The pump probe process is therefore viewed not as a transition between different states, but rather as a scattering between quasiparticles, single-excitons, resulting from their nonboson nature. The HB signal comes from the hole-hole overlap in the ground state and SE and ESA come from particle−particle overlap in the excited state.

III. Time-resolved two Color Pump Probe

The seven lowest energy excitons plus two high energy excitons with large oscillator strength calculated using the Frenkel−Hamiltonian parameters (eq 1)[23] are given in Figure 1 and displayed in Figure 2. For each exciton α the radius of the circle at the center of the segment n is proportional to $\varphi_\alpha(n)$, thus indicating which segments contribute to each exciton. The arrows indicate strength and direction of the corresponding transition dipole moments. The excitons are confined within a single generation. The lowest exciton is nearly completely localized on the perylene unit. The second and third have major contributions from the two units of the first generation. The following four are predominantly formed from second generation segments, whereas the rest (only two examples shown) is distributed over the third and fourth generation. The exciton energies are shown in Figure 3. For clarity, we hereafter report the energies relative to the lowest exciton energy throughout the discussion. $\Delta\omega_\alpha = \omega_\alpha - \omega_0$, where $\omega_0 = 20968$ cm^{-1} is the energy of the perylene trap (exciton 0).

All simulations of exciton dynamics and the pump probe signals were performed at room temperature $T = 300$ *K*. The parameters $\lambda = 70$ cm^{-1} and $\Lambda = 800$ cm^{-1} were taken from ref 18, so that the present pump probe signals can be directly compared with previous simulations of time- and frequency-gated fluorescence.[18] These parameters result in a trapping time of ∼50 ps, which is a typical experimental value. Experimental trapping times upon excitation on the periphery generally depend on the solvent and were determined to be as fast as 10 ps in dichloromethane (but only 80 ps in *n*-hexane).[36]

For simplicity, we use a single dephasing rate $\Gamma = 810$ cm^{-1}, which reproduces the experimental absorption line width.[18] The dephasing rates strongly influence the dynamics, as can be seen from the calculations with narrow line widths given below. Using different rates for various segments will refine the model, and may be required for the analysis of more detailed experiments.

We assume a Gaussian pump pulse envelope with a variance $\sigma = 20$ fs and tuned to $\Delta\omega = 8072$ cm^{-1} to be on resonance with the peripheral excitons. The probe was assumed to be both monochromatic and very short (i.e., in the snapshot limit[32]), allowing to spectrally resolve the signal at variable time delays.

The absolute value of the propagated Doorway wave packet (eq 11) is depicted in Figure 4 in the exciton basis[18]

$$|N_{\alpha\beta}(\tau)| = |\sum_{mn} \varphi_\alpha(m)\varphi_\beta(n)N_{mn}| \qquad (12)$$

The exciton numbering is given in Figure 3. The initially created coherences are completely dephased within 500 fs where the matrix $N_{\alpha\beta}$ becomes diagonal and hereafter we only see population relaxation. The diagonal (population-) terms show an efficient funneling toward the lowest energy exciton, localized at the perylene trap, and after 100 ps the entire wave packet is localized on the perylene. This energy funneling

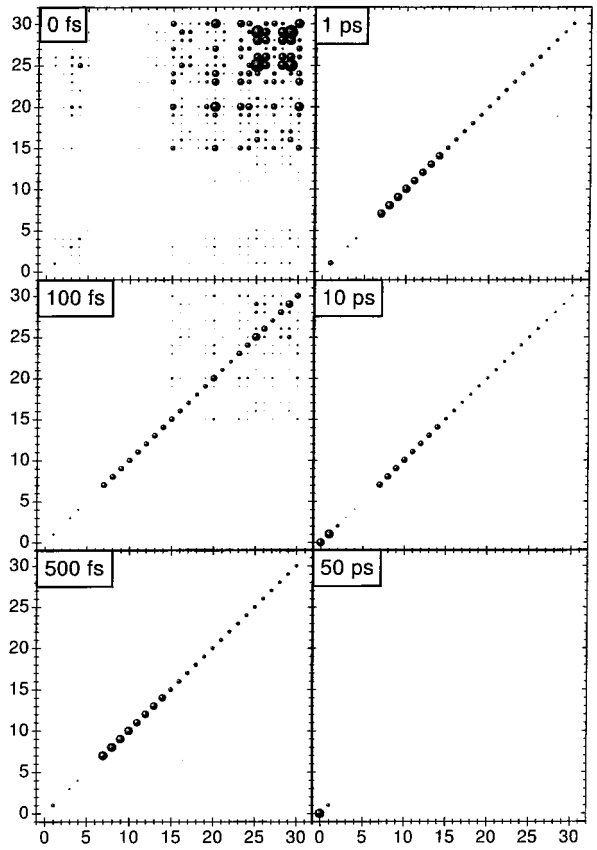

Figure 4. Absolute value of the propagated Doorway wave packet $|N_{\alpha\beta}(\tau)|$ in the exciton representation.

process can be monitored either by time-resolved fluorescence,[18] or by pump−probe experiments,[37] which are the focus of this article.

Figure 5 displays the spectrally resolved pump−probe signal for $\Delta\omega = 8072$ cm^{-1} excitation of the peripheral segments and various delay times, as indicated. Negative signal corresponds to reduced absorption (i.e., increased transmission) due to HB and SE. Positive signals result from ESA. The pump probe technique directly follows the energy funneling since populated exciton states show negative PB signals at the corresponding transition energies. Even though the individual exciton lines are too close to be resolved, we find distinct bands for excitons from different generations. As shown in Figure 2, the exciton-wave functions are mainly localized within one generation and the contributions of different generations can be clearly distinguished. During the first ps, the excitation is localized on the periphery, as indicated by the strong negative signal at ∼8100 cm^{-1}. It then moves toward lower energy sites, gradually populating the second and first generation and finally reaching the perylene trap. The funneling is completed after ∼100 ps where the only negative contribution corresponds to the perylene site. By examining the pump−probe spectra we can directly observe and quantify the funneling process of excitons toward lower energy states.[18]

It is interesting to note that generation 1 seems to be much more involved in the energy transport than generation 2. The coupling from generation 2 to generation 1 ($J_{21} = -325$ cm^{-1}) is larger than $J_{12} = -302$ cm^{-1} or $J_{32} = -158$ cm^{-1}.[23] This might partially explain why generation 2 is only weakly populated throughout the energy funneling on a purely kinetic level. This feature must be related to coherence effects in our Redfield equations treatment. The dynamics need not be sequential as expected from simple kinetic equations.

Although HB and SE result exclusively from single exciton states, and thus follow the exciton dynamics in the same way as time-resolved fluorescence, the positive ESA signals are a new feature of the pump probe technique. In the exciton state picture, the ESA probes transitions from one to two-exciton states. In the chromophore representation, this means that the excitation of one chromophore changes the absorption of a different chromophore due to their mutual interaction; this change directly shows up in the nonlinear pump probe signal and is directly reflected in the scattering matrix which shows that to generate a signal there must be interaction between the segments involved.

The two-exciton states can generally be expanded as[21]

$$|\tilde{\alpha}\rangle = \sum_{m,n} \Psi_{\alpha}(m, n) B_m^{\dagger} B_n^{\dagger} |g\rangle \tag{13}$$

The two-exciton wave functions Ψ_α are proportional to the imaginary part of the two-exciton variables[21] $Y_{mn}(\omega) \equiv \int d\tau \exp[i\omega\tau]\langle B_m(\tau)B_n(\tau)\rangle$, where $B_m(\tau)$ is the annihilation operator of the m'th segmental site in the Heisenberg representation. By using a small dephasing rate γ, Y_{mn} can be calculated using the exciton scattering matrix Γ_{mn} and the single-exciton wave functions $\varphi_\alpha(n)$[21]

$$Y_{mn}(\omega_1 + \omega_2) = \frac{1}{(\omega_1 - \Omega)^2} \sum_{n',n''} \bar{\Gamma}_{n,n''}(\omega_1 + \omega_2) \times \sum_{\alpha,\beta} \frac{\varphi_\alpha(n')\varphi_\beta(n')\varphi_\alpha(m)\varphi_\beta(n)}{\omega_1 + \omega_2 - \epsilon_\alpha - \epsilon_\beta + i\gamma} \tag{14}$$

where Ω is an average single-exciton energy.

The information about the two-exciton resonances originating from interactions between excitons is contained in the poles of the scattering matrix. From eq 14, we see that the two-exciton wave function contains contributions of all pairs of single exciton wave functions that interact via the scattering matrix $\bar{\Gamma}_{nm}$ (eq A11). The energies of the relevant two-exciton states obtained from the poles of the scattering matrix together with the one-exciton energies are displayed in Figure 3.

The temporal evolution of the signal for three frequencies in the region of the trap, generation 1 and the peripheric units (generations 3 and 4), shown in Figure 6, clearly reflects their coupled dynamics. At the highest energy (dotted curve), corresponding to the frequency of the excitation pulse, we find an instantaneous bleaching-signal induced by the excitation, which gradually decays to zero. The signal at the resonance frequency of the perylene (full curve) shows a PB component which slowly builds up as the excitation funnels toward the trap. The most interesting behavior resulting from the combined effect of several processes is found in the intermediate (generation 1) energy region (dashed curve). We first see the buildup of a bleaching signal as these sites get populated by energy transfer from the higher energy sites. Then the amplitude decreases as the population is transferred further to the perylene. Finally, a strong positive signal builds up, resulting from excited-state absorption from the lowest (trap) single exciton state to two-exciton states.

To identify the various contributions to the transient absorption signal of Figure 5, we repeated the simulations with a narrow ($\Gamma = 8$ cm^{-1}) line width keeping all other parameters the same. Figure 7 shows the resulting pump probe signal.

The small dephasing strongly affects the calculated dynamics. The lines are narrow and all bands (especially of generation 1

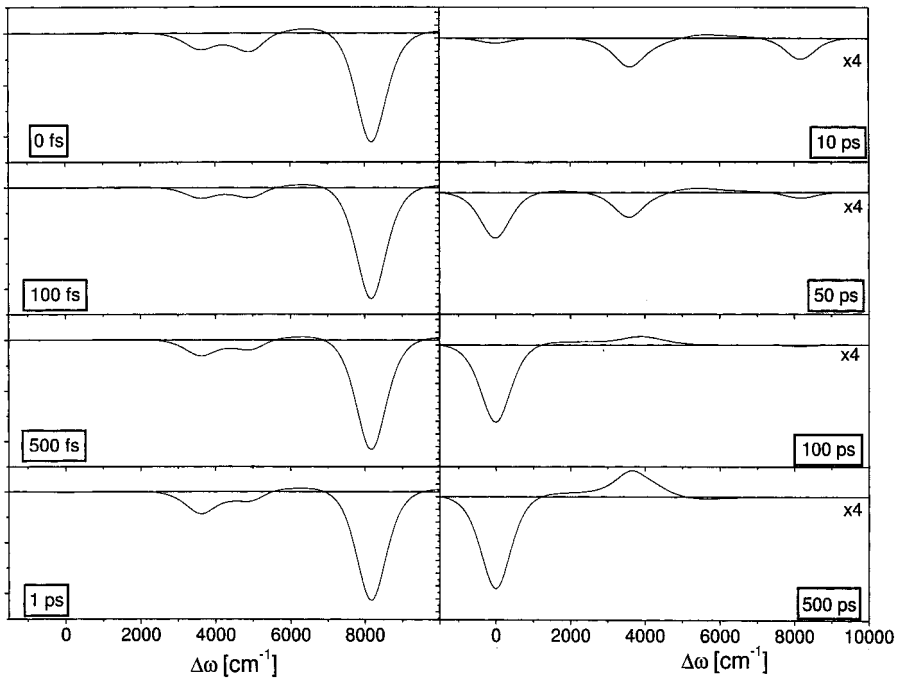

Figure 5. Spectrally resolved Pump−Probe Signal for different time delays ($\Gamma = 810$ cm^{-1}). Note that the signals at long times are multiplied by a factor of 4.

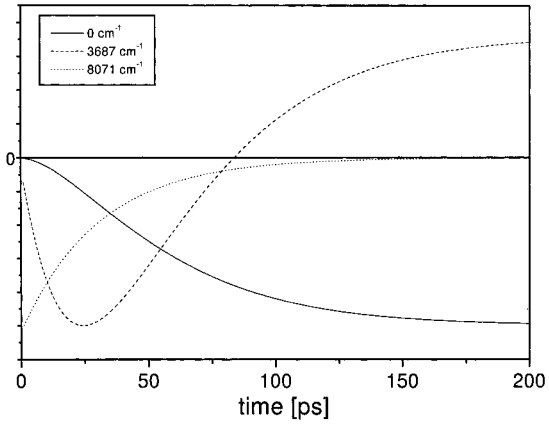

Figure 6. Pump-probe signal vs the delay time for three probe energies, as indicated. Same parameters as in Figure 5

and 2) are spectrally separated. Thus, the transfer from generation 2 to 1 is slowed and we expect the funneling processes to proceed in a more sequential fashion between neighboring generations only. Indeed, in Figure 7 generation 2 appears to be much more significantly populated compared to Figure 5. Simulations with artificially narrow bandwidth are very helpful for identifying the different contributions.

Initially, the excitation is localized on the peripheral high energy units and we see a sharp progression of predominantly bleaching and stimulated emission contributions in this region. There are 24 exciton states localized in generations 3 and 4 on the blue edge of the spectrum. (Some of them are degenerated and not all energies are resolved.) Within a few ps, generations 1 and 2 are populated and again we observe an interplay of positive and negative contributions, but now in the region around $\Delta\omega \approx 5000$ cm^{-1}. The lines have a dispersive profile and the ESA contributions are energetically very close and overlap with the SE and HB contributions.

The nonlinear signal originates from the interactions or scattering between the various segments. In our Hamiltonian, we did not include direct long range dipole couplings between excitons and the only coupling is due to Pauli exclusion (nonboson character of excitons). Consequently, $\bar{\Gamma}_{nm}$ is localized and only contains off diagonal elements between adjacent segments which make a contribution to the signal. For example, in Figure 7, initially, when the peripheral units are excited, we do not observe ESA in the perylene region. Because there is only very weak interaction and no direct scattering between these two-excitations which reside on a distant generation, they do not directly influence the absorption of the trap and there is no nonlinear signal in its vicinity.

The insets of Figure 7 show regions around three dominant lines that correspond to the PB signal of the trap and excitons 1 and 2 for a time delay of 100 ps with high resolution, $\Gamma = 0.8$ cm^{-1}. Let us focus on one of the peaks and discuss it in more detail. The $\Delta\omega = 3659$ cm^{-1} line corresponds to exciton 2 (see Figure 3). Within 10 ps this exciton is strongly populated as can be deduced from the pump−probe signal and verified from the doorway wave packet depicted in Figure 4. At 50 ps the population attains a maximum and then slowly decreases. At the same time an ESA signal appears on the high energy edge of this transition. From the inset of Figure 7 we note the $\Delta\omega = 3709$ cm^{-1} transition, corresponding to the energy difference between the fourth two-exciton and the third single-exciton state. We can attribute it to the following event: exciton 3 ($\Delta\omega_3 = 4998$ cm^{-1}) is excited and the probe subsequently undergoes excited state absorption to a two-exciton state, which has the major contributions only of excitons 2 and 3. Note also the increased ESA bandwidth because the dephasing of the two-exciton state is involved. A similar pattern can also be found at the exciton 3 band (last inset). At 100 ps most of the excitation is localized on the trap so that influences of different excitons on the trap absorption are small. However, we see its influences on excitons 1 and 2 through the two 3709 cm^{-1} and 3659 cm^{-1} excited-state absorption bands discussed above.

IV. Stationary Pump−Probe Line Shapes

In the previous section, we demonstrated that the time-resolved pump probe technique may be effectively used to

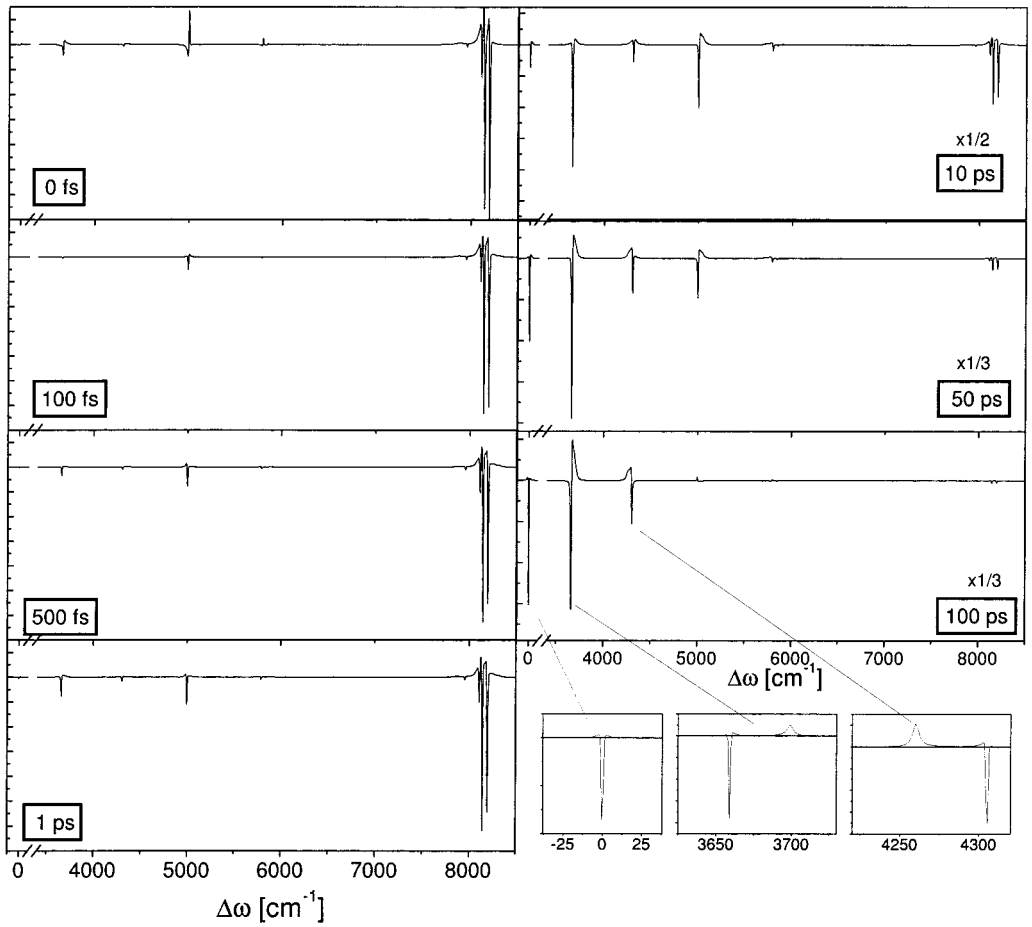

Figure 7. Pump-probe signal for different time delays. Parameters are identical to Figure 5 except for a narrower line width ($\Gamma = 8$ cm^{-1}). Some signals were multiplied by the factors indicated. The inset shows the region around several peaks for $\tau = 100$ ps and $\Gamma = 0.8$ cm^{-1} on an expanded scale.

investigate the coupling and energy transport as well as the two-exciton states. Information about two exciton states may also be obtained from frequency-domain four wave mixing signals, described by the nonlinear susceptibility $\chi^{(3)}$

$$\chi^{(3)}(-\omega_s;\omega_1,\omega_2,\omega_3) = \frac{1}{6}\sum_{\text{perm}}\sum_{mijk}\mu_m\mu_i\mu_j\mu_k \times \sum_{nl} G_{mn}(\omega_s)G_{li}(\omega_1)G_{lj}(\omega_2)G^{\dagger}_{kn}(-\omega_3)\bar{\Gamma}_{nl}(\omega_1+\omega_2) + \text{c}'.\text{c}'. \tag{15}$$

Here c′.c′. stands for complex conjugation and change of the signs of all frequencies, perm denotes summation over the six permutations of frequencies ω_1, ω_2, and ω_3. μ_m denotes the transition dipole moment of the m'th segment, G is the one-exciton Green function, and $\bar{\Gamma}_{nl}$ is the two-exciton scattering matrix as given in the appendix. This expression only describes the coherent part of $\chi^{(3)}$ which is sufficient for studying the coupling among sites.[38] Population relaxation is neglected.

The pump−probe signal is generated by two beams in the direction $\boldsymbol{k_s} = \boldsymbol{k_1} - \boldsymbol{k_1} + \boldsymbol{k_2}$ and is given in frequency domain by the imaginary part of the third-order susceptibility $W_{pp}(\omega_1,\omega_2) = \text{Im}[\chi^{(3)}(-\omega_2;\omega_1,\omega_2, -\omega_1)]$. The two exciton states can directly be probed by two-photon absorption, where both frequencies ω_1 and ω_2 are tuned off-resonant with respect to the one-exciton states. Invoking the rotating wave approximation, neglecting the signal's dependence on geometry[39] and assuming equal transition dipole moments of all chromophores μ we get

$$S_{\text{pp}} \propto \mu^4 \text{Im}\sum_{m,n}\bar{\Gamma}_{mn}(\omega_1+\omega_2) \tag{16}$$

The two-exciton state energies shown in Figure 2 were calculated from the poles of eq 16.

Calculations of the third-order susceptibility were performed using the same parameters as for the time-resolved pump probe spectra. However, to better show how the coupling is revealed in the frequency domain calculations, we did not include the population relaxation and damping. Figure 8(a) shows W_{pp} which corresponds to the frequency domain pump−probe signal. It was calculated for the same parameters as the time-resolved pump−probe signals and for a dephasing $\Gamma = 810$ cm^{-1}. To amplify the positive off-diagonal bands, the positive scale is 10 times finer than the negative one. Individual single-exciton lines are not resolved but we find again broad bands corresponding to contributions from different generations. The two-dimensional plot of $\chi^{(3)}$ vs ω_1 and ω_2 reveals strong negative peaks at the one-exciton energies along the diagonal ($\omega_1 = \omega_2$) resulting from bleaching of the single exciton bands. Coupling between different sites leads to positive off-diagonal ESA peaks.

To identify the contributions of the individual excitons, we have also calculated the high-resolution third-order susceptibility, assuming $\Gamma = 8$ cm^{-1}, as depicted in Figure 9(a). The left column shows the imaginary part on a linear scale. Since the different contributions span several orders of magnitude, the dominant peaks are off scale in order to better see some of the weaker features. The right column shows the absolute value of the optical susceptibility $|\chi^{(3)}|$, plotted on a logarithmic scale.

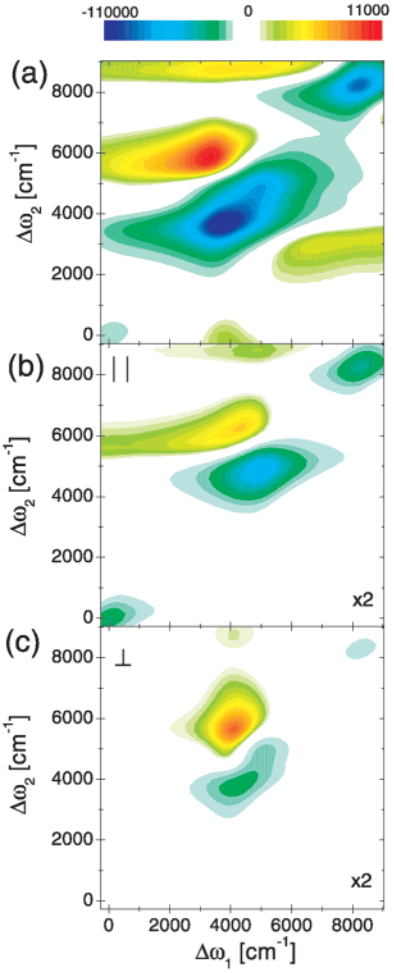

Figure 8. Frequency domain pump probe absorption (imaginary part of $\chi^{(3)}$) for the same parameters used in Figure 5: (a) unpolarized pulses; (b) parallel || configuration; (c) perpendicular ⊥ configuration. In both cases the pump is parallel to the transition dipole moment of the trap. The probe is either parallel || or perpendicular ⊥ to the pump.

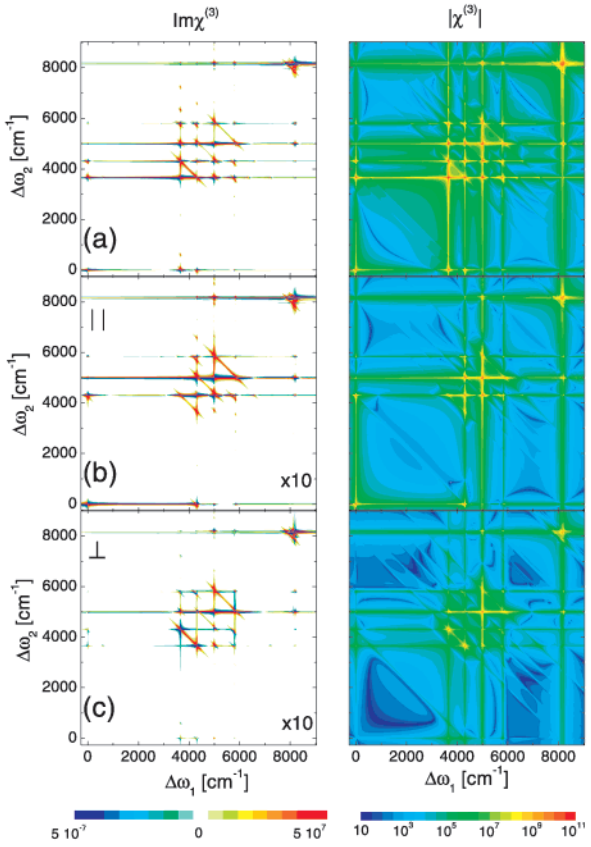

Figure 9. $\chi^{(3)}$ calculated using the same parameters of Figure 7: (a) unpolarized pulses; (b) parallel || configuration; (c) perpendicular ⊥ configuration. Left column: the imaginary part. Right column: absolute value on a logarithmic scale. (Arbitrary units.)

Although the imaginary part of the nonlinear susceptibility directly corresponds to the pump−probe signal, the absolute value and the real part can be measured in heterodyne transient grating experiments. From Figure 9(a), we see that W_{pp} has negative bands along the diagonal at all exciton energies, resulting from PB. The 2D plots show a complex pattern since the real and imaginary parts of the linear response are mixed in third order. There are positive antidiagonal features if the sum of the pump and probe pulse frequencies coincides with a two-exciton state energy, i.e., $\omega_1 + \omega_2 = \omega_{fg}$. These correspond to two photon absorption and are strongly enhanced if one of the frequencies is resonant with a single exciton energy. These weaker features are clearly seen in the logarithmic plot of $|\chi^{(3)}|$.

To more closely examine the coupling between sites, we display several sections of Figure 9 where ω_1 is taken to be resonant with different excitons. In Figure 10 (a) the excitation is resonant with the highest energy exciton and causes a strong bleaching signal at this frequency. We further see signals at the energies of all other generation 3 and 4 excitons. However, we also see smaller influences on the excitons of the first and second generation whose coupling to the trap is orders of magnitudes smaller. Figure 10(b), where ω_1 is resonant with exciton 2, shows that this generation is relatively strongly

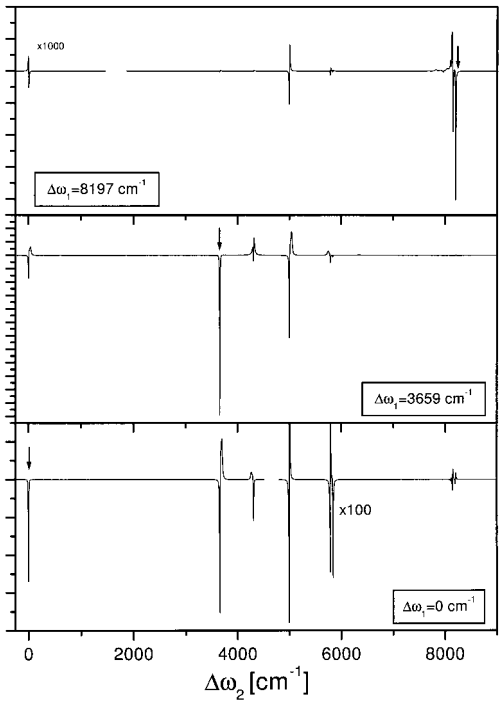

Figure 10. Sections of the imaginary part Im$\chi^{(3)}$ (Figure 9(a)) vs ω_2 for different fixed values of ω_1.

coupled to the perylene unit (exciton 1). This is confirmed by Figure 10(c), where ω_1 is tuned on resonance with exciton 1 and we find a strong signal at the exciton 2 energy.

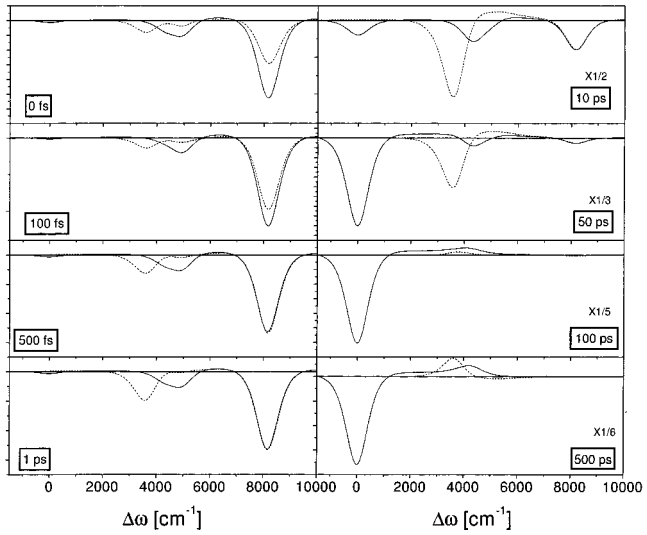

Figure 11. Spectrally resolved pump−probe signal for different time delays using polarized pulses. In both cases the pump is parallel to the transition dipole moment of the trap. The probe is either parallel || (full line) and perpendicular ⊥ (dashed line) to the pump.

V. Polarized Pump Probe Spectroscopy

Additional information can be obtained by using polarized pulses and oriented samples. Figure 11 shows the pump probe signal for different time delays, when the pump is polarized parallel to the dipole of the perylene site and the probe is either parallel || or perpendicular ⊥ to the pump. Again, we can observe the energy funneling and the various generations show distinct bleaching signals once they are populated. In the parallel case, we finally get a strong bleaching from the trap together with a weak ESA signal. The perpendicular case offers a quite different view of the same funneling process. In particular, we see that generations 2 and 3 show up very differently for both polarizations. The main transition dipole of generation 1 (resulting from exciton 1) is perpendicular to the excitation, whereas generation 2 has mainly parallel contributions. Most notably, the trap shows no bleaching signal for the perpendicular polarization and in the long time limit we only see the ESA signal and no PB signal of the trap.

The polarized frequency-domain spectra shown in Figure 8(b) and (c) reveal the same signatures as in the time domain. For the parallel configuration, we see bleaching signals from the trap and the different exciton bands along the diagonal. For the perpendicular configuration the trap is not visible, the negative maximum along the diagonal vanishes and strong bleaching signals are not observed. This can be seen in more detail in the high resolution $\Gamma = 8\ \mathrm{cm}^{-1}$ calculations, shown in Figure 9(b) and (d). In Figure 9(b), where the pump and probe are parallel to the trap dipole no diagonal signal at the exciton 2 energy is observed because its dipole moment is perpendicular to the pulse polarization. Nevertheless off-diagonal peaks indicate a coupling between this state with exciton 3, which is not directly observed in this configuration. In the perpendicular configuration (Figure 9(b)) no diagonal peak of the trap or excitons 2 and 3 can be observed because their dipole moment is orthogonal either to the pump or to the probe. Signatures of these excitons can still be found in the off-diagonal peaks.

In conclusion, the calculations presented in this paper show that pump−probe spectroscopy can give valuable information about the dynamics of complex extended chromophore aggregates such as the nanostar. The nonlinear exciton equations were used in conjunction with the doorway-windows formalism to simulate time-resolved transient absorption spectra, which show the energy funneling, but also yield additional information about interactions between different segments and the two-exciton states. We further calculated and analyzed the signatures of the couplings between chromophores in two-dimensional frequency domain four wave mixing for different pulse polarization configurations.

Acknowledgment. The support of the chemical science division, department of energy, is gratefully acknowledged. A.T. was funded by the Austrian Special Research Program F016 "ADLIS" (Austrian Science Foundation Vienna/Austria).

Appendix A: The Snapshot Signal

The doorway and the window wave packet can be separated into the left (L) and right (R) components[32]

$$\mathscr{D}_{kl}(\tau-\tau',\omega_1) = \mathscr{D}_{kl,L}(\tau-\tau',\omega_1) + D_{kl,R}(\tau-\tau',\omega_1) \quad \text{(A1)}$$

and

$$\mathscr{W}_{mn}(\tau-\tau',\omega_2) = \mathscr{W}_{mn,L}(\tau-\tau',\omega_2) + \mathscr{W}_{mn,R}(\tau-\tau',\omega_2) \quad \text{(A2)}$$

These components can be expressed in terms of their snapshot limit counterparts $\mathscr{D}^0_{mn,\alpha}(t)$ and $\mathscr{W}^0_{mn,\alpha}(t)$ and the Wigner spectrograms for the laser pulses F_α and I_α, with $\alpha = L, R$. These expressions have a similar form

$$\mathscr{D}_\alpha(\tau-\tau',\bar{\omega}_1) = \int_0^\infty \mathrm{d}t_1 \int_{-\infty}^{\infty} \frac{\mathrm{d}\omega}{2\pi} \mathscr{D}^0_\alpha(t_1) I_\alpha(\tau-\tau',\omega_1-\omega) \times \exp(is_\alpha \omega t_1) \quad \text{(A3)}$$

$$\mathscr{W}_\alpha(\tau-\tau',\omega_2) = \int_0^\infty \mathrm{d}t_1 \int_{-\infty}^{\infty} \frac{\mathrm{d}\omega}{2\pi} \mathscr{W}^0_\alpha(t_1) \times F_\alpha(\tau-\tau',\omega-\omega_2) \exp(is_\alpha \omega t_1) \quad \text{(A4)}$$

and $s_L = -s_R = 1$.

The Doorway and the Window are written in terms of G and $\bar{\Gamma}$ (where we neglect $G^{(N)}$ in the window wave packet since exciton relaxation is typically slow compared to the dephasing time)

$$\mathscr{D}^0_{kl,L}(t_1) = \sum_p \mu_l \mu_p G_{kp}(t_1) \quad \text{(A5)}$$

$$\mathscr{D}^0_{kl,R}(t_1) = \sum_p \mu_p \mu_k G^*_{lp}(t_1) \quad \text{(A6)}$$

and

$$\mathscr{W}^0_{mn,L}(t_1) = \sum_{qrj} \mu_q \mu_r \int_0^{t_1} \mathrm{d}\tau'' \int_0^{\tau''} \mathrm{d}\tau' G_{qj}(t_1-\tau'') \times \bar{\Gamma}_{jm}(\tau''-\tau') G^*_{jn}(\tau''-\tau') G_{mr}(\tau') \quad \text{(A7)}$$

$$\mathscr{W}^0_{mn,R}(t_1) = \sum_{qrj} \mu_q \mu_r \int_0^{t_1} \mathrm{d}\tau'' \int_0^{\tau''} \mathrm{d}\tau' G^*_{qj}(t_1-\tau'') \times \bar{\Gamma}^*_{jm}(\tau''-\tau') G_{jn}(\tau''-\tau') G^*_{nr}(\tau') \quad \text{(A8)}$$

The one-exciton Green functions G_{mn} represent the propagator of the exciton variable $\langle B \rangle$

$$G_{mn}(t) = i\theta(t) \langle m| \mathrm{e}^{-iH_e t - \Gamma t} |n\rangle \quad \text{(A9)}$$

or equivalently in the frequency domain (after a Fourier

transform)

$$G_{mn}(\omega) = -\sum_{\alpha} \frac{\varphi_{\alpha}(m)\varphi_{\alpha}(n)}{\omega - \epsilon_{\alpha} + i\Gamma} \tag{A10}$$

where Γ is the exciton dephasing rate.

$\bar{\Gamma}_{jj',pp'}(\tau'' - \tau')$ is the exciton−exciton scattering matrix which, in the frequency domain has the following form for the present model (eq 1)[40]

$$\bar{\Gamma}_{jj',pp'}(\omega_2) = \delta_{jj'}\delta_{pp'}\bar{\Gamma}^{(0)}_{jp}(\omega_2) \tag{A11}$$

More general expressions for $\bar{\Gamma}^{(0)}_{jp}$ are given in refs 32 and 25 which for two level systems reduce to[40]

$$\bar{\Gamma}^{(0)}_{jp}(\omega_2) = -[G^{(2)}(\omega_2)]^{-1}_{jp} \tag{A12}$$

where the unperturbed two-exciton Green function is given by

$$G^{(2)}_{jp}(\omega_2) = \frac{1}{\hbar}\sum_{\alpha\beta} \frac{\varphi_{\alpha}(j)\varphi_{\beta}(j)\varphi_{\alpha}(p)\varphi_{\beta}(p)}{\omega_2 - \epsilon_{\alpha} - \epsilon_{\beta} + 3i\Gamma} \tag{A13}$$

The pump−probe signal in the snapshot limit[41] is obtained by setting the Wigner spectrograms of the pump and the probe pulse to

$$I_{\alpha}(\tau - \tau', \omega_1 - \omega) = \delta(\tau - \tau')\delta(\omega_1 - \omega) \tag{A14}$$

$$F_{\alpha}(\tau - \tau', \omega - \omega_2) = \delta(\tau - \tau')\delta(\omega - \omega_2) \tag{A15}$$

The time integrations in eq 10 can then be carried out and the pump−probe signal then assumes the form

$$S_{\mathrm{pp}}{}^{0}(\omega_2, \tau; \omega_1) = \sum_{mnkl} \mathscr{W}'^{0}_{mn}(\omega_2) G^{(N)}_{mn,kl}(\tau) \mathscr{D}^{0}_{kl}(\omega_1) \tag{A16}$$

where all snapshot quantities are labeled by a 0 superscript. $\mathscr{D}^{0}_{kl}(\omega_1)$ and $\mathscr{W}'^{0}_{mn}(\omega_2)$ are the Fourier transforms of $\mathscr{D}^{0}_{kl}(t_1)$ and $\mathscr{W}'^{0}_{mn}(t)$

$$\mathscr{D}^{0}_{kl}(\omega_1) \equiv \int_{-\infty}^{\infty} \mathrm{d}t \mathrm{e}^{\mathrm{i}\omega_1 t} \mathscr{D}^{0}_{kl}(t) \tag{A17}$$

$$\mathscr{W}'^{0}_{mn}(\omega_2) \equiv \int_{-\infty}^{\infty} \mathrm{d}t \mathrm{e}^{i\omega_2 t} \mathscr{W}'^{0}_{mn}(t) \tag{A18}$$

with

$$\mathscr{D}^{0}_{kl}(t) = \mathscr{D}^{0}_{kl,L}(t) + \mathscr{D}^{0}_{kl,R}(t) \tag{A19}$$

$$\mathscr{W}'^{0}_{mn}(t) = \mathscr{W}'^{0}_{mn,L}(t) + \mathscr{W}'^{0}_{mn,R}(t) \tag{A20}$$

References and Notes

(1) Bosman, A. W.; Janssen, H. M.; Meijer, E. W. *Chem. Rev.* **1999**, *99*, 1665.

(2) Jockusch, S.; Ramirez, J.; Sanghvi, K.; Nociti, R.; Turro, N. J.; Tomalia, D. A. *Macromolecules* **1999**, *32*, 4419; Schwarz, P. F.; Turro, N. J.; Tomalia, D. A. *J. Photochem. Photobiolog. A* **1998**, *112*, 47.

(3) Gilat, S. L.; Adronov, A.; Fréchet, J. M. J. *Angew. Chem., Int. Ed. Engl.* **1999**, *38*, 1422; Gilat, S. L.; Adronov, A.; Fréchet, J. M. J. *J. Org. Chem.* **1999**, *64*, 7474.

(4) Issberner, J.; Moors, R.; Vögtle, F. *Angew. Chem.* **1994**, *106*, 2507; *Angew. Chem., Int. Ed. Engl.* **1994**, *33*, 2413.

(5) Archut, A.; Vögtle, F.; De Cola, L.; Azzellini, G. C.; Balzani, V.; Ramanujam, P. S.; Berg, R. H. *J. Eur. Chem.* **1998**, *4*, 699. Archut, A.; Azzellini, G. C.; Balzani, V.; De Cola, L.; Vögtle, F. *J. Am. Chem. Soc.* **1998**, *120*, 12 187. Balzani, V.; Campagna, S.; Denti, G.; Juris, A.; Serroni, S.; Venturi, M. *Acc. Chem. Res.* **1998**, *31*, 26.

(6) Venturi, M.; Serroni, S.; Juris, A.; Campagna, S.; Balzani, V. *Topics in Current Chemistry* **1998**, *197*, 193.

(7) Webber, P.-W.; Liu, Y.-J.; Devadoss, C.; Bharathi, P.; Moores, L. S. *Adv. Mater.* **1996**, *8*, 237.

(8) Junge, B. M.; McGrath, D. V. *Chem. Commun.* **1997**, *9*, 857; Tomalia, D. A.; Naylor, A. M.; Goddard, W. A. *Angew. Chem., Int. Ed. Engl.* **1990**, *29*, 138.

(9) Pugh, V. J.; Hu, Q.-S.; Pu, L. *Angew. Chem., Int. Ed.* **2000**, *39*, 3638.

(10) Kopelman, R.; Shortreed, M.; Shi, Z−Y.; Tan, W.; Xu, Z.; Moore, J.; Bar-Haim, A.; Klafter, J. *Phys. Rev. Lett.* **1997**, *78*, 1239.

(11) Swallen, S. F.; Shi, Z−Y.; Tan, W.; Xu, Z.; Moore, J. S.; Kopelman, R. *J. Lumin.* **1998**, *76−77*, 193.

(12) Shimoi, Y.; Friedman, B. A. *Chem. Phys.* **1999**, *250*, 13.

(13) Devadoss, C.; Bharathi, P.; Moore, J. S. *J. Am. Chem. Soc.* **1996**, *118*, 9635; *Macromolecules* **1998**, *31*, 8091.

(14) Bar-Haim, A.; Klafter, J. *J. Chem. Phys.* **1998**, *109*, 5187; *J. Phys. Chem. B* **1998**, *102*, 1662.

(15) Shortreed, M.; Swallen, S. F.; Shi, Z−Y.; Tan, W.; Yu, Z.; Devadoss, C.; Moore, J.; Kopelman, R. *J. Phys. Chem. B* **1997**, *101*, 6318.

(16) Bar-Haim, A.; Klafter, J.; Kopelman, R. *J. Am. Chem. Soc.* **1997**, *119*, 6197.

(17) Raychaudhuri, S.; Shapir, Y.; Chernyak, V.; Mukamel, S. *Phys. Rev. Lett.* **2000**, *85*, 282; Raychaudhuri, S.; Shapir, Y.; Mukamel, S. *Phys. Rev. E* (in press).

(18) Kirkwood, J.; Scheurer, C.; Chernyak, V.; Mukamel, S. *J. Chem. Phys.* **2001**, *114*, 2419.

(19) Nakano, M.; Takahata, M.; Fujita, H.; Kiribayashi, S.; Yamaguchi, K.; *Chem. Phys. Lett.* **2000**, *323*, 249. Takahata, M.; Fujita, H.; Nakano, M.; Kiribayashi, S.; Nagao, H.; Yamaguchi, K. *Nonlinear Optics* **2000**, *26*, 177. Fujita, H.; Takahata, M.; Nakano, M.; Kiribayashi, S.; Nagao, H.; Yamaguchi, K. *Nonlinear Optics* **2000**, *26*, 185.

(20) Tretiak, S.; Chernyak, V.; Mukamel, S. *J. Phys. Chem. B* **1998**, *102*, 3310.

(21) Chernyak, V.; Poliakov, E. Y.; Tretiak, S.; Mukamel, S. *J. Chem. Phys.* **1999**, *111*, 4158.

(22) Poliakov, E. Y.; Chernyak, V.; Tretiak, S.; Mukamel, S. *J. Chem. Phys.* **1999**, *110*, 8161.

(23) Minami, T.; Tretiak, S.; Chernyak, V.; Mukamel, S. *J. Lumin.* **1999**, *87−89*, 115.

(24) Davydov, A. S. *Theory of Molecular Excitations*; Plenum: New York, 1971.

(25) Chernyak, V.; Zhang, W. M.; Mukamel, S. *J. Chem. Phys.* **1998**, *109*, 9587.

(26) Redfield, A. G. *Adv. Magn. Reson.* **1965**, *1*, 1.

(27) Pollard, W. T.; Felts, A. K.; Friesner, R. A. *Adv. Chem. Phys.* Vol. 93 1997; Pollard, W. T.; Friesner, R. A. *J. Chem. Phys.* **1994**, *100*, 5054.

(28) Chernyak, V.; Minami, T.; Mukamel, S. *J. Chem. Phys.* **2000**, *112*, 7953.

(29) Mukamel, S. *Principles of Nonlinear Optical Spectroscopy*; Oxford University Press: New York, 1995.

(30) Kleiman, V. D.; Melinger, J. S.; McMorrow, D. *J. Phys. Chem. B* **2001**, *105*, 5595.

(31) Chernyak, V.; Mukamel, S. *J. Opt. Soc. Am. B* **1996**, *13*, 1302.

(32) Dahlbom, M.; Minami, T.; Chernyak, V.; Pullerits, T.; Sundström, V.; Mukamel, S. *J. Chem. Phys.* **2000**, *104*, 3976.

(33) Chernyak, V.; Mukamel, S. *J. Chem. Phys.* **1996**, *105*, 4565.

(34) Bosma, W. B.; Mukamel, S.; Greene, B. I.; Schmitt-Rink, S. *Phys. Rev. Lett.* **1992**, *68*, 2456.

(35) Yan, Y. J.; Mukamel, S. *Phys. Rev. A* **1990**, *41*, 6485.

(36) Swallen, S. F.; Kopelman, R.; Moore, J. S.; Devadoss, C. *J. Molecular Structure* **1999**, *485−486*, 585.

(37) Tortschanoff, A.; Piryatinski, A.; Mukamel, S. *J. Lumin.* **2001**, *94−95*, 569.

(38) Zhang, W. M.; Chernyak, V.; Mukamel, S. *J. Chem. Phys.* **1999** *110*, 5011.

(39) Chernyak, V.; Poliakov, E. Y.; Tretiak, S.; Mukamel, S. *MRS Proceedings*, edited by Drake, M.; J. Klafter 1998.

(40) Kühn, O.; Chernyak, V.; Mukamel, S. *J. Chem. Phys.* **1996**, *105*, 8586.

(41) Mukamel, S. *J. Chem. Phys.* **1997**, *107*, 4165.